I&EC research
Industrial & Engineering Chemistry Research

Article

pubs.acs.org/IECR

Enhanced Electrically Induced Micropatterning of Confined Thin Liquid Films: Thermocapillary Role and Its Limitations

Hadi Nazaripoor, Charles R. Koch, and Mohtada Sadrzadeh*

Department of Mechanical Engineering, 10-367 Donadeo Innovation Center for Engineering, University of Alberta, Edmonton, Alberta T6G 1H9, Canada

ABSTRACT: Electrohydrodynamic (EHD) and thermocapillary (TC) forces are used to destabilize the interface of ultrathin liquid films and create sub-micrometer-sized features. EHD instabilities result from the normal component of Maxwell stress, while TC forces induce shear stress to the interface. In this study, the accuracy of linear stability (LS) analysis for the prediction of final structures which undergo nonlinear stages during pattern evolution is investigated by using new normalizing factors. The reasons for the deviation between LS analysis and nonlinear simulation results are then discussed. It is found that, despite the positive effect of TC in reducing the structure sizes compared to the EHD case, it causes lateral movement of pillars, which results in faster coarsening in later stages of pattern formation. To control the movement of patterns and create well-ordered features, nonuniform electrostatic and TC-induced instabilities of the film are examined by using ridge and square-block-shaped electrodes.

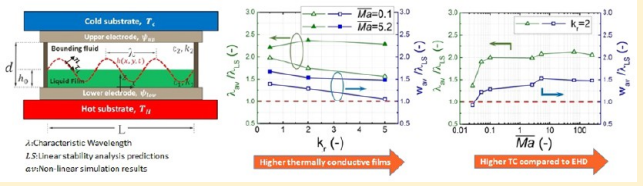

INTRODUCTION

The goal to advance a fast and inexpensive technique for noncontact lithography by employing fluid instabilities leads to a variety of approaches such as self-organized pattern formation by dewetting,[1,2] electrically induced instabilities,[3] and thermally assisted patterning.[4] Development of these instabilities at the film interface leads to pattern formation and/or film disruption, which is of interest in numerous applications. The physical basis for the liquid surface deformation induced by an electric field has been known since its initial observation by Swan.[5] Over 100 years later, Schaffer et al.[6] reported hexagonal ordered micropillar formation when a large electric field ($>10^7$ V/m) was applied to an ultrathin molten polymer film. The center-to-center distance of raised columnar structures, called pillars, which bridged two electrodes was characterized by maximum growth of instabilities in the linear stage mode. Since then, the electrically induced instabilities of thin liquid films have received great attention for the creation of novel micrometer and sub-micrometer structures.[3,7−14] Different approaches has been used to lower the size of the created structures on the film in the electrohydrodynamic (EHD) lithography technique, such as employing alternating current (AC)[9,15,16] instead of direct current (DC); using leaky dielectric,[17,18] ionic conductive,[19,20] and perfect conductive[11] films instead of perfect dielectric polymer films; and working with viscoelastic and non-Newtonian molten polymers.[16,21]

The hydrodynamics of self-organized pattern formation due to Bénard−Marangoni (BM) instability in heated thick liquid films has also been widely studied.[22] The nonuniformity of surface tension induces interfacial shear stress at the interface, which breaks the mechanical equilibrium and leads to a convective motion of fluid. Thermocapillary (TC) instability caused by temperature-dependent interfacial tension in thick and less viscous liquid films leads to the short-wavelength (SW) mode and is responsible for Bénard convection cells.[22] In contrast, the long-wavelength (LW) mode is present in much thinner and more viscous films. In SW mode the interface remains flat, whereas in the LW mode elongations of the interface are observed. Many studies were conducted on the LW instabilities of heated liquid films[23−25] but the generated elongations on the interface had very small height-to-width aspect ratios, and their capture was not of practical interest. However, creation of micro- and nanometer-sized features on ultrathin films was the focus of a few studies. These efforts were initiated by Chou and Zhuang[26] who observed a pattern replication in ultrathin molten polymer films sandwiched between two closely spaced substrates. They did not apply any electric field but proposed the image charge or surface charge (SC)-induced EHD instability model to justify their observations. Soon thereafter, Schaffer et al.[6,27] repeated the same set of experiments but, by grounding the film and substrates, ruled out the SC model as the responsible mechanism for growth of instabilities and micropillar formation. Instead, an acoustic phonos (AP) model was proposed as a dominant mechanism for growth of instabilities which relies on the low-frequency acoustic phonons and the resulting radiation pressure induced to the nanofilms. More recently, Dietzel and Troian[28] and McLeod et al.[29] tested nanofilms confined within closely spaced substrates, and formation of periodic pillar arrays was observed by applying a transverse thermal gradient. Their results are in contrast with the conventional BM instability that requires reaching to a critical Marangoni number.[22,28] They experimentally verified that the growth and amplification of

Received: July 10, 2017
Revised: August 29, 2017
Accepted: August 31, 2017
Published: August 31, 2017

DOI: 10.1021/acs.iecr.7b02814
Ind. Eng. Chem. Res. 2017, 56, 10678−10688

long-wave TC instabilities are responsible for pillar formation in nanofilms, not, as previously hypothesized, electrostatic attraction or acoustic phonons.

Incorporation of tangential TC stress into the normal electrostatic stress in thin films was first examined analytically by Corbett and Kumar[30] using linear stability (LS) analysis. They presented the LS analysis predictions for the fastest-growing waves of perfect dielectric (PD) and leaky dielectric (LD) films in the presence of a large thermal gradient and electric field for 1D films. Later, Nazaripoor et al.[31] performed the 2D nonlinear analysis to study the dynamics and morphological evolution of liquid nanofilms under combined TC-EHD instabilities. Increasing the TC pressure by increasing the thermal gradient resulted in the formation of more compact structures as compared to the pure EHD patterning. Since the predictions from LS are based on initial growth of instabilities, one main question investigated in this paper is the accuracy of the LS analysis for the prediction of the final formed structures which undergo nonlinear stages during pattern evolution. The limiting stage for the minimum structure size formation at the interface is also investigated. To do this, the role of the thermal conductivity of a film in enlarging the TC stress and its consequences on pattern evolution for both linear and nonlinear analysis are discussed in the next sections. Experiments in the literature[7,32] have shown that the electric breakdown results in the formation of larger size structures and unevenly distributed patterns which are not captured in the theoretical predictions focused on the EHD pattering of nanofilms.[33−35] The TC force is added to the electrostatic force to allow use of a lower applied electric field and avoid electric breakdown in the film and the bounding layer.

In electrically induced patterning, a patterned mask is commonly used to minimize the coarsening effects and create well-ordered structures. The effect of the protrusions' shape (strip, square, and triangle block protrusions)[36−39] and their size on the fidelity of pattern replication is well studied for PD,[33,34,40,41] LD,[42] and ionic conductive[20] films both experimentally and numerically. Here, we also examine the use of patterned masks (top electrode) to induce nonuniform electrostatic and thermocapillary forces to control both shape and size in combined TC-EHD pattern formation of nanofilms.

MATHEMATICAL MODEL

A two-dimensional schematic of the three-dimensional ultrathin liquid film sandwiched between two electrodes is shown in Figure 1. Transverse electric field induces *Maxwell* stress

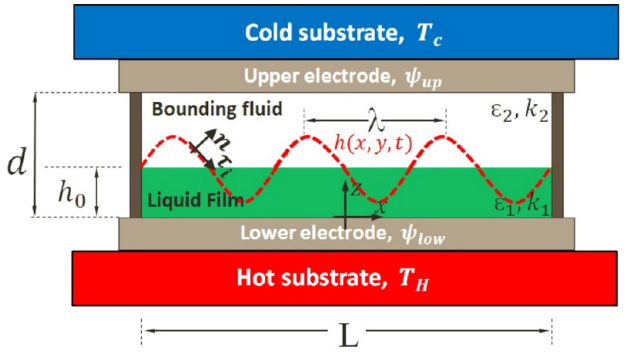

Figure 1. A 2D schematic of the ultrathin liquid film sandwiched between top (cold) and bottom (hot) electrodes.

normal ($\mathbf{n}$) to the interface due to mismatch of electrical properties of liquid film and the bounding fluid. The tangential ($\boldsymbol{\tau}_i$) TC stress is the result of the thermal gradient across the film as the liquid film is heated from below (T_H) and cooled from above (T_C). The liquid film is considered as an incompressible Newtonian fluid since the shear rate in the growth of instabilities is very small. Mass conservation and momentum and energy balances govern the dynamics and pattern formation process. Considering the long-wave approximation, the spatiotemporal evolution of thin liquid films subjected to the transverse electric field and thermal gradient is described by the following dimensionless equation,[25]

$$\frac{\partial H}{\partial \tau} + \nabla\left(H^3\nabla P - \frac{3H^2}{2}\nabla\Gamma\right) = 0 \tag{1}$$

where $H = H(X,Y,\tau)$ is the nondimensional interface height and $\nabla = (\partial/\partial X, \partial/\partial Y)$. The variable $\Gamma = (\epsilon h_0/\mu u_c)\gamma$ is the dimensionless interfacial tension, and $P = \epsilon h_0/\mu u_c(p + \phi)$ is the dimensionless pressure in which p represents the capillary pressure and $\phi = -\rho g z + \phi_{LW} + \phi_{EL}$ accounts for the contributions of hydrostatic pressure, Lifshitz−van der Waals intermolecular interactions, and electrostatic pressure. Dimensionless time is $\tau = (3u_c/\lambda)t$, and u_c is the characteristic lateral speed due to either individual TC and EHD flow or their combination. The film density $\rho = \rho(T_H)$ and viscosity $\mu = \mu(T_H)$ are assumed constant. It is also assumed that the electrodes are perfect thermal conductors and there is no heat loss within the electrodes.

The second term in eq 1 shows the superposition effect in growth of instabilities and changes due to the variations in hydrostatic forces ∇P and interfacial tension $\nabla\Gamma = (d\Gamma/dT)\nabla T$. Interfacial tension is approximated to be a linear function of temperature ($\gamma = \gamma_0 - \alpha_T(T - T_0)$). $\alpha_T > 0$ is the surface tension gradient and γ_0 and T_0 are the reference interfacial tension and temperature, respectively.

The lateral coordinates are normalized with λ ($X, Y = x/\lambda, y/\lambda$), and the vertical coordinate, interface height, and distance between electrodes are scaled with film initial thickness h_0 ($Z = z/h_0$, $H = h/h_0$, and $D = d/h_0$). Variable $\epsilon = h_0/\lambda$ ($\ll 1$) is the dimensionless ratio of initial film thickness to the characteristic lateral length scale, which confirms the validity of the long-wave approximation.

Since the pressure within the film is constant (according to lubrication theory), its value is found by considering the normal stress balance at the interface. Lifshitz−van der Waals intermolecular interactions $\phi_{LW} = -A/6\pi H^3$ are considered when the film thickness is less than 100 nm,[43] and A is the effective Hamaker constant defined for the three-layer system. For the perfectly dielectric films, under long wave approximation, the electrostatic pressure, ϕ_{EL}(N m^{-2}), simplifies to[6]

$$\phi_{EL} = -\frac{1}{2}\varepsilon_0\varepsilon_1(\varepsilon_r - 1)\left[\frac{\psi_{up}}{h(1 - \varepsilon_r) + \varepsilon_r d}\right]^2 \tag{2}$$

where $\varepsilon_r = \varepsilon_1/\varepsilon_2$ is the relative dielectric constant, ε_1 (ε_2) is the relative dielectric constant of the bottom (top) layer, ε_0 is the vacuum dielectric constant, and ψ_{up} is the applied electric potential. Given these, the hydrostatic term in eq 1 becomes

$$\nabla P = \mathrm{Ca}^{-1}\nabla^3 H - \mathrm{Ca}^{-1}\mathrm{Bo}\nabla H + \nabla(\Phi_{LW} + \Phi_{EL}) \tag{3}$$

DOI: 10.1021/acs.iecr.7b02814
Ind. Eng. Chem. Res. 2017, 56, 10678−10688

where Ca = $\mu u_c/(\epsilon^3\gamma)$ is the Capillary number, Bo = $\rho g\lambda^2/\gamma$ is the Bond number, and Φ_{LW} and Φ_{EL} are dimensionless Lifshitz−van der Waals and electrostatic pressures, respectively.

Temperature is normalized as $\Theta = (T - T_C)/(T_H - T_C)$, and a simplified energy equation is solved considering conduction as the dominant mechanism of heat transfer.[31] The resulting temperature distribution along the interface is given by $\Theta|_{Z=H} = k_r(D - H)/[(1 - k_r)H + k_rD)]$, and $k_r = k_1/k_2$ is the relative thermal conductivity of layers (k_1 (k_2) is the thermal conductivity of the bottom (top) layer). Substituting the temperature distribution into the TC pressure term yields

$$\nabla\Gamma = \frac{\mathrm{Ma}k_rD}{[(1 - k_r)H + k_rD]^2}\nabla H = \nabla\Phi_T \tag{4}$$

where Ma = $\epsilon\alpha_T\Delta T/\mu u_c$ is the Marangoni number and $\Delta T = T_H - T_C$ is the maximum temperature difference. The characteristic lateral velocity, u_c, is found by setting the interface height, its slope, and the TC stress (in eq 4) to unity. The dimensionless TC pressure term is $\Phi_T = (\epsilon h_0/\mu u_c)\phi_T$. In dimensional form, the TC pressure, ϕ_T (N m^{-1}), is as follows:

$$\phi_T = \frac{3}{2}\frac{k_r\alpha_T d\Delta T}{(1 - k_r)[(1 - k_r)h + k_r d]} \tag{5}$$

Substituting eqs 3 and 4 into eq 1 yields the thin-film equation, which provides the spatiotemporal evolution of the film under both EHD and TC forces:[31]

$$\frac{\partial H}{\partial\tau} + \nabla(H^3[\mathrm{Ca}^{-1}\nabla^3 H - \mathrm{Ca}^{-1}\mathrm{Bo}\nabla H - \nabla(\Phi_{LW} + \Phi_{EL})]) - \nabla(H^2\nabla\Phi_T) = 0 \tag{6}$$

Experimental studies on EHD and TC of ultrathin liquid films (thickness < 500 nm),[6,29] showed that Capillary number and Bond number are of the order of $O(10^1)$ and $O(10^{-5})$, respectively. Hence, the contribution of gravity to the hydrostatic pressure is neglected compared to other forces in eq 6. In derivation of eq 6, it is assumed that (i) there is no electric breakdown in both liquid film and the bounding layer, (ii) the solvent evaporation is completed before the onset of TC and EHD patterning process, and (iii) the viscosity of molten polymer at temperatures above the glass transition $T > T_g$ is constant over the evolution time.

Scaling of Thin-Film Equation. In the absence of thermal gradient and electrostatic force, LW forces are the most dominant source for growth of instabilities in ultrathin films.[25] Equation 6 is rescaled using $L_s = h_0^2/(2\pi\gamma/A_L)^{1/2}$ for spatial coordinates ($X = x/L_s$, $Y = y/L_s$), $T_s = A_L^2/12\,\pi^2\mu\gamma h_0^5$ for time ($\tau = t/T_s$), and $\Phi_s = 2\pi h_0^3/A_L$ for pressure ($\Phi = (p + \phi)/\Phi_s$). In the absence of electric field ($\psi_{up} = 0$), the TC is dominant in heated films when both viscous scaling (eq 6)[29,44] and LW scaling[23] have been used to normalize the TC pressure. For the EHD-induced instabilities under isothermal conditions, the electrostatic pressure is considered as dominant[6] and eq 6 is rescaled using factors of $L_s = (\gamma\varepsilon_2^2h_0^3/0.5\varepsilon_0\varepsilon_1(\varepsilon_1 - \varepsilon_2)\psi_{up}^2)^{1/2}$, $T_s = 3\mu\gamma\varepsilon_2^2h_0^3/[0.5\varepsilon_0\varepsilon_1(\varepsilon_1 - \varepsilon_2)\psi_{up}^2]$, and $\Phi_s = 0.5\varepsilon_0\varepsilon_1(\varepsilon_1 - \varepsilon_2)\psi_{up}^2/\varepsilon_2^2h_0^2$. Here, the EHD scaling factors for the combined TC-EHD instabilities are used, and the thin-film equation is revised. In the TC-EHD-induced instabilities, the electrostatic pressure is dominant,[30,31] and thus eq 6 is rescaled with $X = x/L_s$, $Y = y/L_s$, $\tau = t/T_s$, and $\Phi = (p + \phi)/\Phi_s$ using $L_s = (\gamma\varepsilon_2^2h_0^3/0.5\varepsilon_0\varepsilon_1(\varepsilon_1 - \varepsilon_2)\psi_{up}^2)^{1/2}$, $T_s = 3\mu\gamma\varepsilon_2^2h_0^3/[0.5\varepsilon_0\varepsilon_1(\varepsilon_1 - \varepsilon_2)\psi_{up}^2]$, and $\Phi_s = 0.5\varepsilon_0\varepsilon_1(\varepsilon_1 - \varepsilon_2)\psi_{up}^2/\varepsilon_2^2h_0^2$. The resulting normalized TC-EHD thin-film equation is as follows:

$$\frac{\partial H}{\partial\tau} + \nabla(H^3\nabla^3 H - H^3[\nabla(\Phi_{LW} + \Phi_{EL})]) - \nabla(H^2\nabla\Phi_T) = 0 \tag{7}$$

Linear Stability Analysis. Linear stability (LS) analysis is used to predict the characteristic wavelength for the growth of instabilities λ. Experimental studies on EHD[6] and TC[29] showed that the center-to-center distance of pillars (observed at initial stages of formation) compared favorably with the maximum wavelength for growth of instabilities at micrometer-size patterns. The corresponding wavelength is found by replacing the interface height in eq 7 with a small periodic perturbation of the interface about initially flat base state, $H = 1 + \xi\exp[\kappa(X + Y)i + S(\kappa)\tau)]$. In this relation, $\kappa = 2\pi L_s/\lambda$ is the wavenumber, $S(\kappa)$ is the growth coefficient, and ξ ($\ll 1$) is the infinitesimal amplitude coefficient. The following dispersion relation for growth rate is found after neglecting all nonlinear terms: $S(\kappa) = -\kappa^2[\kappa^2 + \partial\Phi_{EL}/\partial H + \partial\Phi_T/\partial H]$.

Over time, the perturbations are amplified if $S > 0$. Since both $\partial\Phi_{EL}/\partial H < 0$ and $\partial\Phi_T/\partial H < 0$, all modes with $\kappa < \kappa_c = (-\partial\Phi_{EL}/\partial H - \partial\Phi_T/\partial H)^{(1/2)}$ are unstable. The fastest growing wave, λ_{max}, corresponding to dominant wavenumber will eventually dominate and is given by

$$\lambda_{max} = 2\pi L_s\left[\frac{\varepsilon_r - 1}{[1 + \varepsilon_r(D - 1)]^3} + \frac{\overline{\mathrm{Ma}}k_rD}{[1 + k_r(D - 1)]^2}\right]^{-1/2} \tag{8}$$

where the modified Marangoni number, $\overline{\mathrm{Ma}} = 3\alpha_T\nabla T/2h_0\Phi_s$, is the ratio of interfacial force gradient to the electrostatic force. To numerically examine this, a liquid film viscosity $\mu = 1$ Pas, interfacial tension $\gamma = 0.048$ N/m, interfacial tension gradient $\alpha_T = 48 \times 10^{-5}$ N/m·K, vacuum dielectric constant $\varepsilon_0 = 8.85 \times 10^{-12}$ C/V·m, dielectric constants of the liquid film $\varepsilon_1 = 2.5(-)$ and the bounding layer $\varepsilon_2 = 1$, 4.16(−), effective Hamaker constant $A_L = -1.5 \times 10^{-21}$ J, and electrodes distance $d = 200$ nm are chosen.

RESULTS AND DISCUSSION

Examining the terms of eqs 7 and 8 shows the inclusion of the TC shear stress could enhance total disturbance of the interface compared to the EHD basecase. In Figure 2, the scaled TC pressure and electrostatic pressure distribution over the interface height are compared for different thermal conductivity and dielectric constant ratios. Having a film with higher thermal conductivity and electrical permittivity compared to the bounding fluid ($k_r > 0$, $\varepsilon_r > 1$), results in negative pressures which means the resulting force pull the interface toward the top electrode (or cold plate). Although both TC and electrostatic pressures (absolute value) increase over the interface height, the change in the TC pressure is negligible compared to the electrostatic pressure.

Linear Stability Analysis. From LS analysis, λ_{max} in eq 8 is a function of applied voltage, initial film thickness, electrodes (or hot and cold substrates) distance, relative dielectric constant between the film and bounding layer, thermal conductivity ratio, and surface tension gradient. In conventional EHD patterning, a variety of methods have been used to lower the structure size from the micrometer to sub-micrometer level.

DOI: 10.1021/acs.iecr.7b02814
Ind. Eng. Chem. Res. 2017, 56, 10678−10688

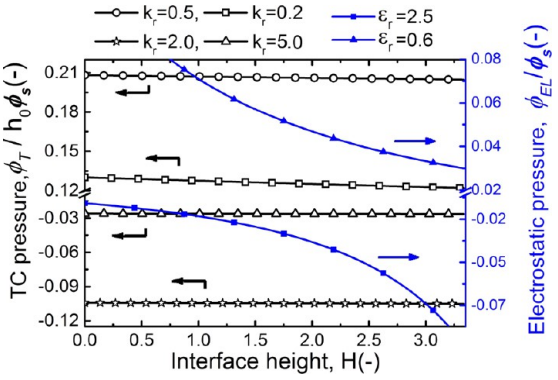

Figure 2. Scaled thermocapillary (TC) tangential pressure (left axis and black lines) and electrostatic pressure (right axis and blue lines) distribution over the interface height.

These methods include increasing the applied voltage;[6] enhancing the electrical conductivity of polymer film by using leaky dielectric (LD),[17,18] ionic conductive,[19] and perfect conductive (PC) materials;[11] replacing the upper gas layer with another polymer layer to reduce the electric potential drop;[7,45] or decreasing the damping interfacial tension at the interface.[46] Except for the last one, the aim is to enhance the net electrostatic force acting normal to the interface.

LS analysis (Figure 3a) show that EHD and TC forces induce different trends to the characteristic wavelength. However, in both EHD and TC, thinner systems (d and h_0) lead to smaller structure size. In this study, the electrodes distance, d, is kept constant and thus an increase in the initial film thickness, h_0 implies higher filling ratio (initial film thickness to the electrodes distance, h_0/d). As the initial film thickness increases, λ_{max} decreases linearly in the pure EHD case while increasing parabolically in the pure TC case. In the combined TC−EHD case, λ is more affected by TC for the lower range of h_0 whereas for the higher values of h_0, EHD is dominant. A parabolic change of λ_{max} with h_0 is observed for k_r = 2, while in cases with k_r < 1 the maximum wavelength escalates linearly as h_0 increases in Figure 3b,c. The smaller filling ratio results in smaller structures for the wide range of k_r. In Figure 3a−c, the temperature difference and applied voltage were kept constant. To find the minimum expected size for λ_{max}, the extreme conditions of temperature gradient and applied potential (ΔT = 100 °C and ψ_{up} = 50 V) are compared with the lower parameter values in Figure 3d. For the filling ratio of 0.3, the minimum characteristic wavelength obtained in k_r = 0.5. The thermal conductivity ratio of layers is found to be more effective at lower voltage and temperature gradient. At ΔT = 100 °C, increasing the electrostatic forces does not affect the λ_{max} compared to ΔT = 25 °C.

Nonlinear Simulations. *Numerical Scheme.* The thin-film equation (eq 7) is a fourth-order nonlinear partial differential equation (PDE) and is solved numerically to find the dynamics and morphology of interface under combined TC-EHD-induced fluid flow. First, spatial derivatives are discretized using finite difference to convert the PDE to a differential algebraic equation (DAE) in time. Differential algebraic solver (DASSL) with an adaptive time stepping is then used for the DAE system.[47] A square domain with size of (4 × 4) λ_{max}^2 (in some cases: (6 × 6) λ_{max}^2) with uniform Cartesian grids of 91 × 91 (121 × 121) and periodic boundary conditions are chosen. Details about the numerical scheme are given in ref 31.

Selecting Domain Size. To show the effect of proper choice for the domain size in nonlinear simulation, the 3D snapshots of the patterns formed on the interface are compared for two different domain sizes, one based on the EHD characteristic

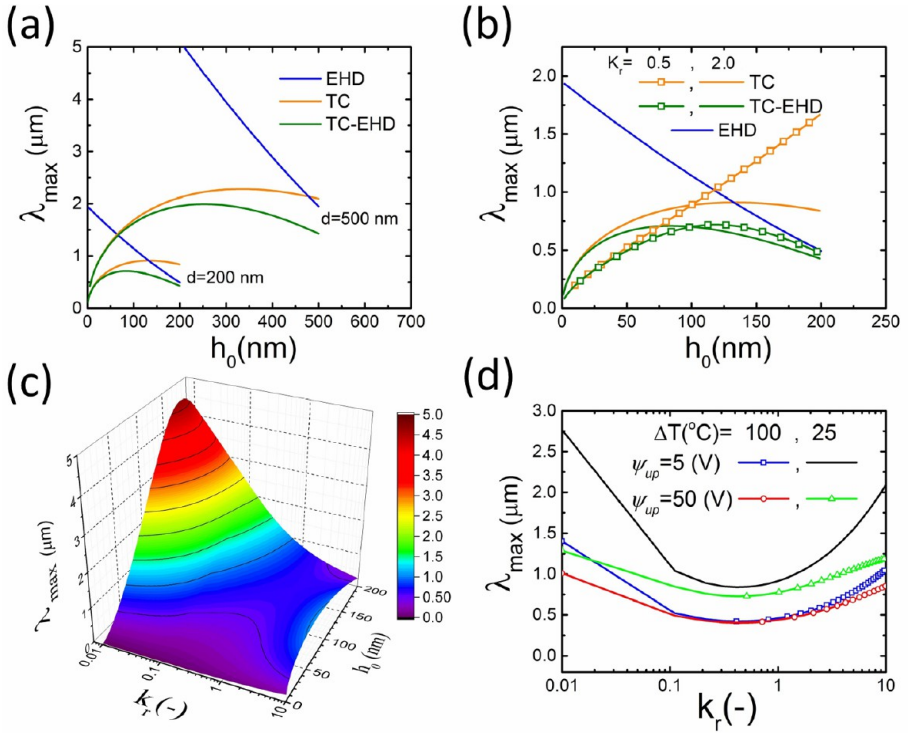

Figure 3. Linear stability analysis predictions for maximum wavelength for growth of instabilities λ_{max}, role of (a) initial film thickness h_0 for two electrode distances, (b) thermal conductivity ratio k_r, (c) combined h_0 and k_r, and (d) temperature difference ΔT and applied voltage ψ_{up}.

DOI: 10.1021/acs.iecr.7b02814
Ind. Eng. Chem. Res. 2017, 56, 10678−10688

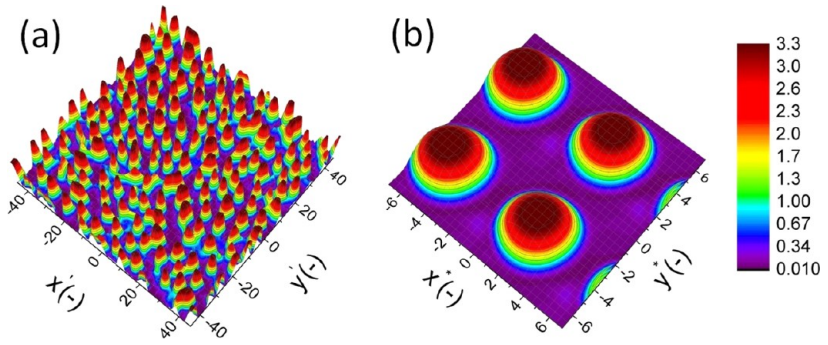

Figure 4. 3D snapshot of quasi-steady state of the formed pattern in the TC-EHD case in the domain area of $4L \times 4L$: (a) $L = \lambda_{EHD}$ and (b) $L = \lambda_{TC\text{-}EHD}$. Other conditions: h_0 = 60 nm, d = 200 nm, ΔT = 100 °C, k_r = 2, ε_r = 2.5, and ψ_{up} = 5 V.

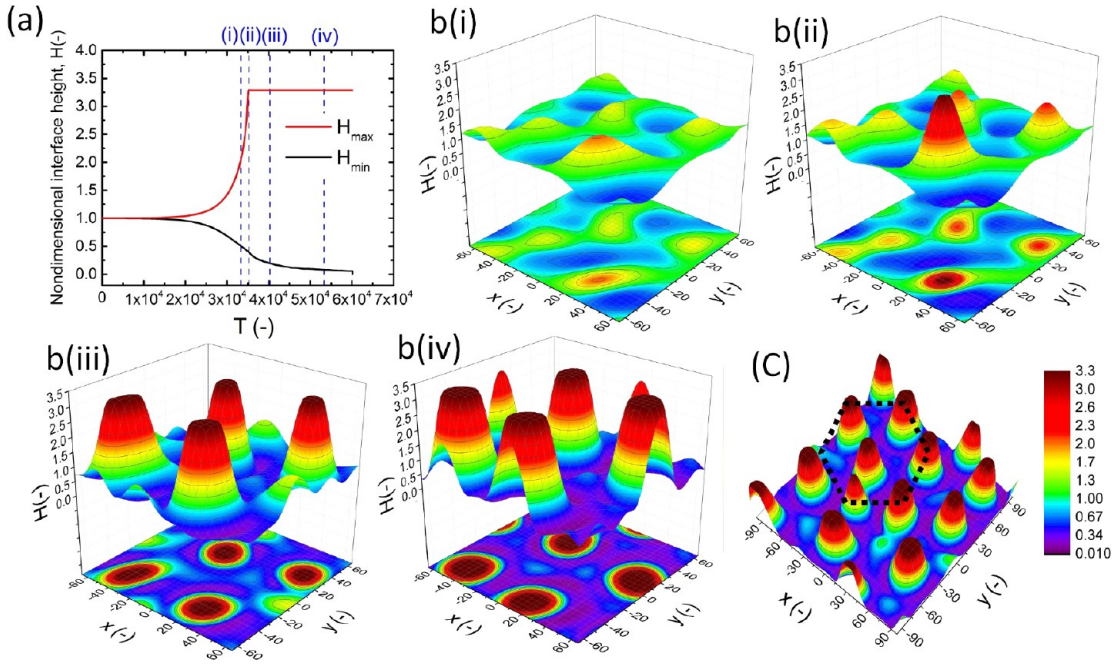

Figure 5. (a)Nondimensional interface height $H(-)$, variations versus nondimensional time $T(-)$. (b) (i–iv) 3D and 2D snapshots of the interface structure over time. (c) 3D snapshot of the interface structure in $6\lambda \times 6\lambda$ domain at quasi steady state. Conditions: h_0 = 60 nm, $\overline{Ma}$ = 0, k_r = 2. Nondimensional times for the 3D plots are $T(-) = 6.6 \times 10^4$ (b(i)), 7.6×10^4 (b(ii)), 1×10^5 (b(iii)), 1.4×10^5 (b(iv)), and 4×10^4 (c).

wavelength (shown in Figure4a) and the other combined TC-EHD wavelength (shown in Figure4b). The EHD characteristic wavelength, λ_{EHD}, can be found by setting $\overline{Ma}$ = 0 in eq 8.

In our previous work,[31] the λ_{EHD} was used for the domain size which is found inefficient due to computational errors and long CPU times. As can be seen in Figure 4b, the structures are packed densely which requires much higher number of grid points (171 × 171) compared the TC-EHD case (91 × 91 for the (4 × 4) λ^2 domain area. To show the effect on the CPU time reduction, the first domain size required solving of 29 241 coupled ODEs at each time step whereas the second domain size only requires solving of 8281 ODEs (around 3.5 times lower number of equations) which results in lower simulation time. Hence, in this study the TC-EHD length scale (λ_{max} in eq 8) is used when thin film is subjected to both electrical and thermal gradients.

Spatiotemporal Evolution of the Film. In the EHD process, the transition from pillars to bicontinuous structure was observed applying filling ratio of h_0/d = 0.5 under uniform electric field.[33] In the case of nonuniform electric field exposure, higher filling ratios has also led to imperfect replication of patterns due to the presence of extra mass of polymer in the system.[35,40] Hence, lower filling ratios received more attention due to their higher potential in faithful replication of patterns. As a result, in the present study, the focus is on the ratios $h_0/d < 0.5$.

The tracking of maximum and minimum interface height over time along with the 3D snapshots of the film interface at different stages of the evolution process are presented in Figure 5. Initial random perturbations reorganize into ridges and valleys and form bicontinuous structures (stage (i)). Then fragmentation occurs and isolated islands are generated. Due to a negative fluid flow diffusion from thinner thickness area to thicker regions, the structures are enlarged and reach top (cold) electrode (stage (ii)). After bridging top and lower electrodes the contact area increases over time to form columnar raised structures with circular cross sections or pillars (stages (iii) and (iv)). Using larger simulation domain area of $6\lambda \times 6\lambda$ reveals the classical hexagonally packed formation of pillars in combined TC-EHD (Figure 5c).

The role of initial film thickness and thermal conductivity ratio in the combined TC-EHD is numerically investigated and

DOI: 10.1021/acs.iecr.7b02814
Ind. Eng. Chem. Res. 2017, 56, 10678−10688

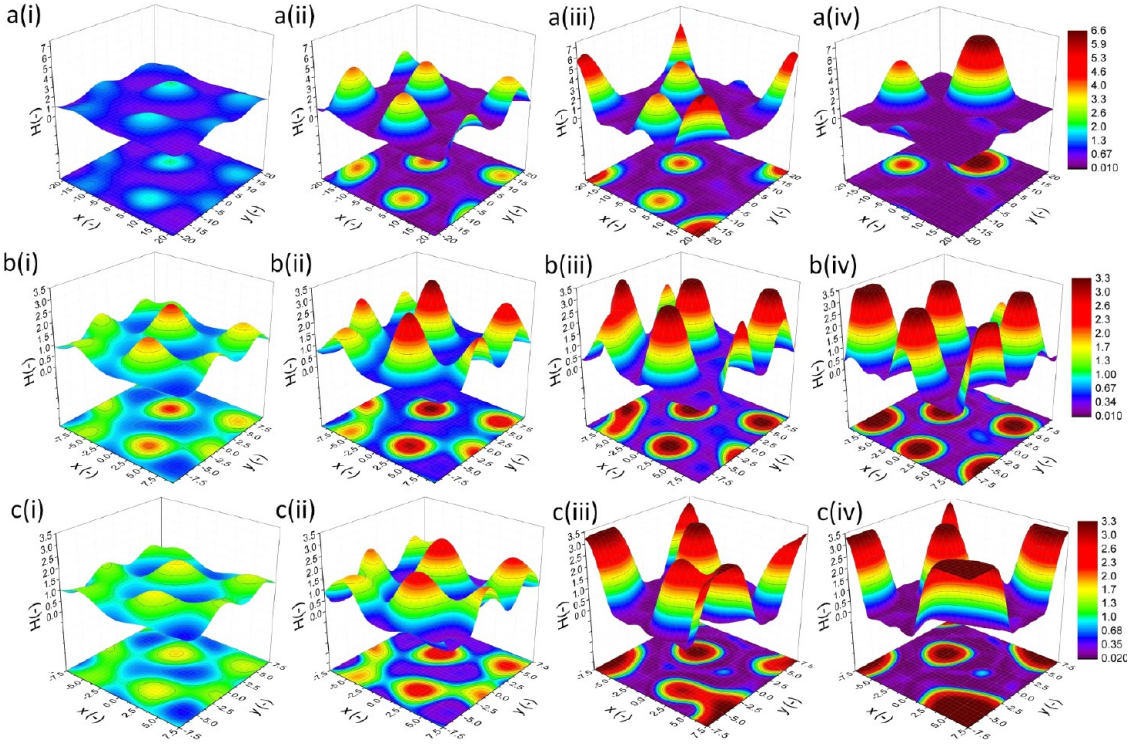

Figure 6. 3D and 2D snapshots of the interface structure over time: (a(i–iv)) h_0 = 30 nm, $\overline{\mathrm{Ma}}$ = 2.6, k_r = 2; (b(i–iv)) h_0 = 60 nm, $\overline{\mathrm{Ma}}$ = 5.2, k_r = 2; and (c(i–iv)) h_0 = 60 nm, $\overline{\mathrm{Ma}}$ = 5.2, k_r = 0.5. Nondimensional times for the 3D plots are $T(-)$ = 604, 872, 1×10^3, and 1.9×10^3 (a(i-iv)); 27, 30, 35, and 45 (b(i–iv)); and 9, 10.5, 14.5, and 16.8 (c(i–iv)).

Table 1. Listing of the Cases and Parameters Considered for Linear and Nonlinear Analysis[a]

				LS analysis	simulation			
ψ_{up} (V)	ΔT (°C)	$\overline{\mathrm{Ma}}$	k_r	λ_{LS} (μm)	pillar density	λ_{av} (μm)	W_{av} (μm)	$\lambda_{av}/\lambda_{LS}$
1	0	0	–	72.41	0.00013	90.3	52.5	1.25
1	25	65	2	1.10	0.205	2.33	1.63	2.12
1	100	260	2	0.55	0.82	1.13	0.81	2.05
5	0	0	–	14.48	0.0045	15.35	10.4	1.06
5*	50	2.6	2	0.6	0.7	1.99	1.38	3.32
5	50	5.2	2	0.78	0.41	1.62	1.20	2.08
5	50	5.2	5	1.01	0.23	2.3	1.5	2.28
5	50	5.2	0.5	0.59	0.63	1.30	0.98	2.20
50	0	0	–	1.45	0.45	1.53	1.04	1.05
50	25	0.026	2	0.88	0.33	1.2	0.82	1.36
50*	100	0.05	2	0.41	1.47	0.78	0.5	1.90
50	100	0.1	2	0.51	1.25	1.03	0.65	2.02
50	100	0.1	5	0.69	0.947	1.07	0.73	1.55
50	100	0.1	0.5	0.40	1.86	0.79	0.55	1.97

[a]Initial film thickness h_0 = 60 nm (except for * cases h_0 = 30 nm).

the results are presented in Figure 6. In films with lower filling ratio (h_0/d = 0.15), first cone shape pillars formed over the domain rather the columnar pillars (image a(ii)). Over time the structures merged together to form larger size pillars that touch the upper cold electrode. Merging of pillars occurs in the later stages of pattern formation in order to lower the energy level of system.[48] This results in coarse large structure formation at the long exposure time to TC-EHD forcing. Using thicker films (h_0/d = 0.3, Figure 6b(i–iv)) shows a similar trend in spatiotemporal evolution of interface as was observed in Figure 5. Based on the LS predictions, the minimum λ_{max} was found for the k_r close to 0.5. Changing k_r from 2 to 0.5 results in a reverse trend in TC pressure acting on the interface. As a result, the pillars tend to merge at earlier stages of pattern formation (image c(ii)). The coalescence of pillars also extends to the later stages (after touching the top electrode) that results in a coarse pattern formation (images c(iii) and c(iv)) at longer times.

The influence of TC on the EHD-induced lithography for reduction of pattern size is examined by using a numerical study for several conditions, and the results are summarized and compared with LS analysis in Table 1. Pillar density is defined

DOI: 10.1021/acs.iecr.7b02814
Ind. Eng. Chem. Res. 2017, 56, 10678–10688

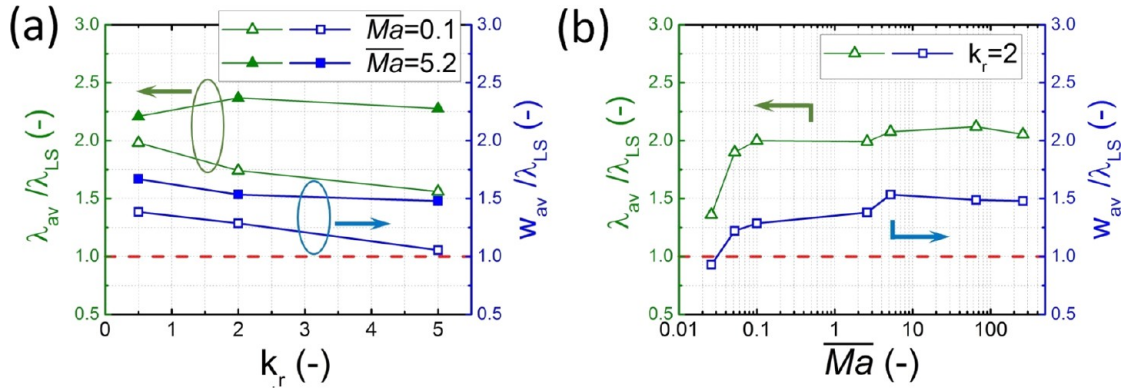

Figure 7. Comparison between averaged center-to-center distance of pillars (λ_{av}) and their average width (W_{av}) from nonlinear simulations with the LS analysis predicted characteristic wavelength (λ_{LS}) for two effective factors of (a) thermal conductivity ratio k_r and (b) modified Marangoni number $\overline{Ma}$.

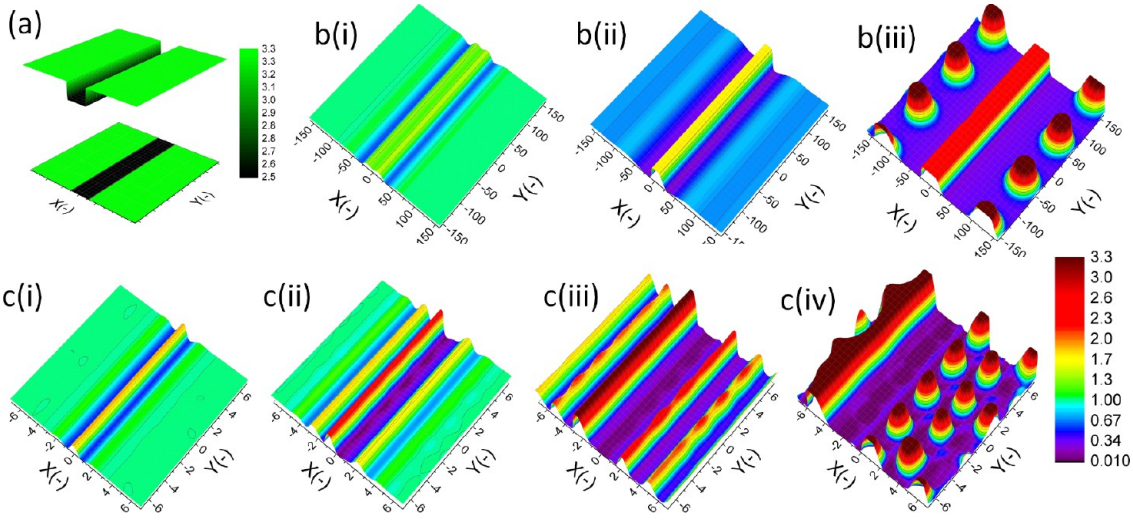

Figure 8. (a) 3D schematic of the upper electrode pattern and 3D snapshots of the formed pattern in (b(i–iii)) EHD ($\overline{Ma}$ = 0) and (c(i–iv)) TC-EHD ($\overline{Ma}$ = 65) induced pattern formation. Nondimensional times are $T(-) = 5.2 \times 10^3$ (b(i)), 3.4×10^4 (b(ii)), and 4.45×10^5 (b(iii)) and 0.02 (c(i)), 0.06 (c(ii)), 0.12 (c(iii)), and 0.25 (c(iv)). Applied voltage, ψ_{up} = 1 V; electrodes distances, d_1 = 200 nm and d_2 = 150 nm; protrusion width, $w_p = \lambda$ = 41.9 μm (b(i–iii)) and 1.1 μm (c(i–iv)); temperature difference, ΔT = 0 °C (b(i–iii)) and 25 °C (c(i–iv)); domain size, $10\lambda \times 10\lambda$ = 0.176 mm^2 (b) and 121.6 μm^2 (c).

as the total number of completely formed pillars in a 1 μm^2 area of patterning domain and is used to show the miniaturization and compactness of the structures. Both linear and nonlinear simulations confirm that an increase in the TC pressure either by increasing temperature difference or by using more thermal conductive films (k_1) results in a higher pillar density and more compact structures compared to the EHD. The center-to-center distance of formed pillars, λ_{av}, and their average width, W_{av}, are compared to the LS analysis predictions, λ_{LS}, for lower and higher relative TC-to-EHD strength of $\overline{Ma}$ = 0.1 and 5.2 (Figure 7a). Ratios of $\lambda_{av}/\lambda_{LS}$ greater than one result in an under prediction of LS and higher nonlinear effects in pattern formation. At lower $\overline{Ma}$, closer agreement is found between the LS predictions and nonlinear simulation results.

The deviation from LS prediction is found to increase when TC has higher strength relative to the EHD (higher $\overline{Ma}$ at constant k_r = 2) as shown in Figure 7b. As $\overline{Ma}$ increases from the pure EHD-induced instabilities ($\overline{Ma}$ = 0), both λ and W ratios increase and finally reach the limiting values of 2 and 1.5 at pure TC-induced patterning condition ($\overline{Ma} \approx 260$), respectively. A possible explanation is the higher merging rate of pillars and coarsening when higher TC tangential stress acts on the interface.

Nonuniform Electrical and Thermal Gradients. A patterned mask is commonly used in the EHD pattering to impose nonuniform electrostatic field to the film and is a successful technique to control both size and shape of features form on the film. Protrusions width and height and their periodicity are effective parameters which should be adjusted accurately to achieve the perfect pattern replication. The material properties of the protrusions plays significant role in pattern replication fidelity[14] which is beyond the scope of this study. Higher electrostatic force is applied to the film under the protrusions (lower electrodes distance region), which results in undulation of the interface toward the electrode. TC force (see eq 5) behaves similarly and it increases when the separation distance of the hot and cold plates decreases. The similarity and differences between EHD and TC-EHD pattern formation under the patterned electrodes will be discussed next. We will investigate the capability of applying nonuniform TC and EHD forces to avoid feature movement which is a main reason for

DOI: 10.1021/acs.iecr.7b02814
Ind. Eng. Chem. Res. 2017, 56, 10678–10688

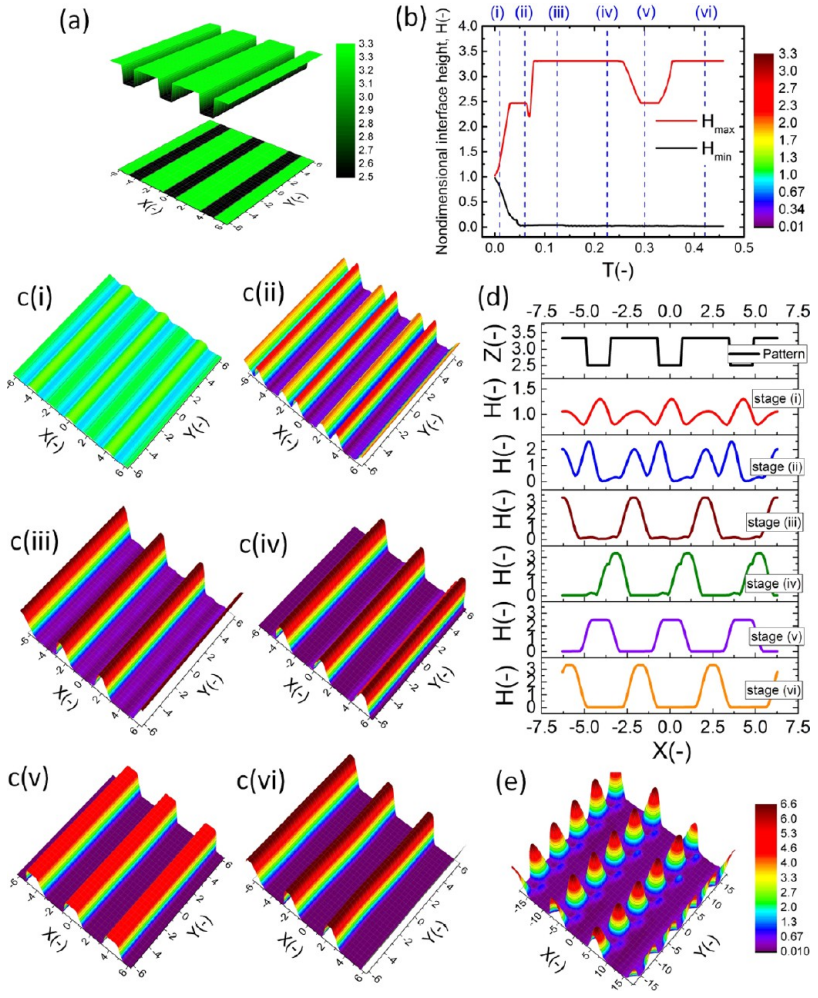

Figure 9. (a) 3D schematic of the upper electrode pattern and (b) nondimensional maximum and minimum interface height profile in TC-EHD patterning. (c(i-vi)) 3D snapshots of the formed pattern and (d) 2D interface height profile of the interface and (e) 3D snapshots of the formed pattern. Initial film thickness, h_0 = 60 nm (b, c, and d) and 30 nm (e). Nondimensional times are $T(-)$ = 0.01 (c(i)), 0.06 (c(ii)), 0.125 (c(iii)), 0.225 (c(iv)), 0.3 (c(v)), 0.42 (c(vi)), and 5 (e). Applied voltage, ψ_{up} = 1 V; electrodes distances, d_1 = 200 nm and d_2 = 150 nm; temperature difference, ΔT = 25 °C; domain size, $9\lambda \times 9\lambda$ = 98.55 μm^2.

the formation of coarse structure in TC-EHD patterning process as discussed above.

EHD- and TC-EHD-induced patterning cases are examined using single ridge protrusion electrode (shown in Figure 8). In both cases, at early stages of the interface evolution (b(i) and c(i)), the interface is pulled toward the top electrode under the protrusion area which is followed by liquid depletion. In the EHD case, the growth of interface height then continues over time and reached the top electrode (image b(ii)). Afterward the secondary pattern formation (image b(iii)) is initiated in regions with lower applied electric field which is observed both numerically and experimentally.[20,33,40] However, in the TC-EHD case, the induced pattern moves parallel to the electrode while the amplitude of secondary induced waves is also increasing and generates undulations parallel to the initial formed ridge (image b(ii)). Over time the initially formed ridge moves from center to the boundary of the domain until it touches the top electrode. The secondary undulations still have lower height (image c(iii)) and after the fragmentation they form pillars aligned parallel to the initial ridge (image c(iv)). The traveling of initial formed pattern adds more complexity to finding a proper mask design in the TC-EHD compared to the EHD base case.

Next, multiple ridges electrode with thickness of λ and the center-to-center distance of 3λ is used to impose the nonuniform electrostatic and thermocapillary forces to the film. The electrodes distances and other conditions remain unchanged. The maximum interface height profile is tracked over time to show multiple stages in pattern evolution (Figure 9,). The stages (i)−(iv) are presented using 3D snapshots of the interface (images c(i−iv)) and 2D height profile along the X-axis (image d). Similar to the single ridge case, at very early stages (stage (i)), the roll-like patterns form under both high- (under the ridges) and low-pressure regions. These undulations grow while they are moving in the direction normal to their alignment until they merge at low-pressure regions (stages (ii) and (iii)). They continue to move and collide with the ridges (stage (iv)), which results in a step-like edge at the crest. They then squeeze under the protrusions which results in thicker undulations as their height is bounded to the lower electrodes distance of d_2 (stage (v)). Over time they move farther and form ridges with higher height-to-width ratios (in stage (vi)) similar to those initially formed in stage (iii). From this stage on, the pattern evolution repeats through stages (iii)−(vi), as shown in Figure 9d. Using films with lower initial thickness of 30 nm leads to the formation of a row of pillars instead of

DOI: 10.1021/acs.iecr.7b02814
Ind. Eng. Chem. Res. 2017, 56, 10678−10688

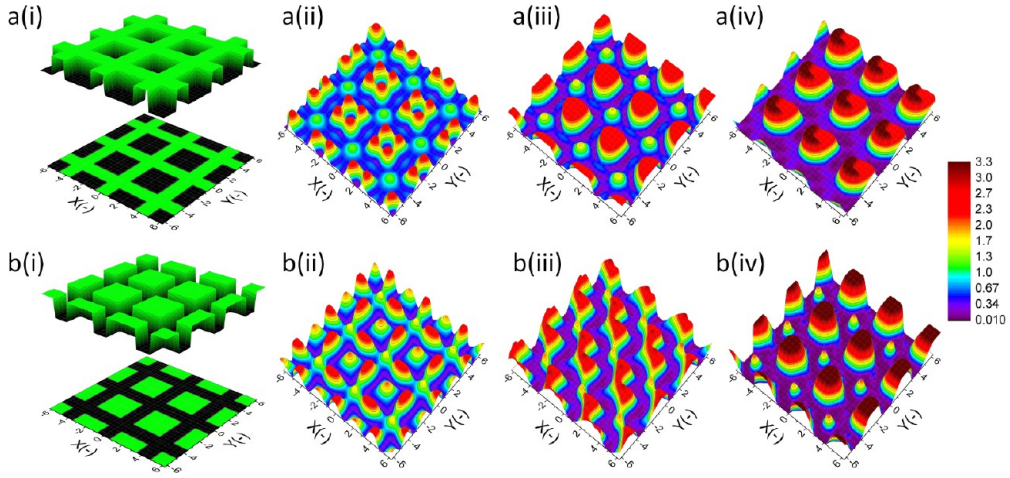

Figure 10. 3D schematic of the upper electrode pattern and the formed structure in TC-EHD-induced pattern formation for (a(i–iv)) positive and (b(i–iv)) negative electrode patterns. Early and quasi-steady stage of pattern formed in (c(i,ii)) positive and (d(i,ii)) electrode patterns. Initial film thickness, h_0 = 60 nm; nondimensional times, $T(-)$ = 0.03 (a(ii)), 0.06 (a(iii)), 0.25 (a(iv)), 0.03 (b(ii)), 0.06 (b(iii)), and 0.25 (b(iv)); applied voltage, ψ_{up} = 1 V; electrodes distances, (a) d_1 = 150 nm and d_2 = 200 nm and (b) d_1 = 200 nm and d_2 = 150 nm; temperature difference, ΔT = 25 °C; domain size, $9\lambda \times 9\lambda$ = 98.55 μm^2.

undulations with the same electrode size and pattern as shown in Figure 9e.

So far, using ridge shape protrusions is found effective in controlling the TC-EHD traveling patterns in one direction while the formed patterns are still moving normal to the ridge alignment. A square block pattern is another common shape which is used in the literature[33,40] to create well ordered patterns. In what follows, we examine both positive (block protrusions) and negative (block defects) patterns on the TC-EHD spatiotemporal evolution as well as the shape at quasi-steady stage (shown in Figure 10). The width of the blocks and their center-to-center distance are set to 2λ. The electrodes distances d_1 and d_2 and the other parameters are kept constant to impose the same electrostatic and TC forces as before. The only change is the distribution of the forces over the domain area. Under the block protrusions (in positive pattern (image a(i)), four cone shape pillars is formed at early stages (image a(ii)) and merged together (image a(iii)). Up to this point, pillars have not moved and patterns were formed under the protrusions (except those small bumps were formed under low pressure regions). Then they move in diagonal direction along $Y = X$ plane and at the subsequent stages the small bumps merge to the larger size pillars.

Under the negative exposure (using square block defects), a different sequence is observed (shown in Figure 10b(i–iv)). Since the applied pressure is lower under the blocks only one cone shape pillar is formed. On the ridges, in between blocks, (higher applied pressure area) larger size oval shape pillars are formed (image b(ii)). Soon after, the generated patterns start moving which results in diagonally aligned bicontinues features (shown in image b(iii)). The movement of patterns ocurs at an earlier stage of pattern evolution compared to the positive electrode pattern. At later stages, pillars are formed which fill the square blocks and remain stable for a long time. In general, the created patterns on the film using the negative exposure are found to be more stable (without movement) for a longer time.

■ CONCLUSIONS

Thermocapillary (TC) and electrohydrodynamic (EHD) long-wave-induced instabilities in ultrathin liquid film are studied using both linear stability (LS) analysis and nonlinear simulation. Both linear and nonlinear analysis showed that the addition of TC shear flow to the EHD-induced flow in ultrathin films reduces the pattern size forming on the film. Nonlinear simulation of the thin-film equation is required for accurate prediction of final shape and size of structures. The LS analysis typically underestimates the center-to-center distance of pillars and their width for the final formed structures of the cases studied. The deviation of the nonlinear analysis from LS analysis predictions increases when the TC force has higher relative strength to the EHD force as a result of a higher tendency for structures to coarsen.

In order to eliminate the movement of patterns in TC-EHD pattern formation, nonuniform force exposure by using patterned mask (top electrode) is examined. Electrodes with single and multiple ridges and square block patterns with both positive and negative exposures are investigated. Although the nonuniform exposure of the TC-EHD forces results in formation of ordered features and postpone the coarsening of structures, the patterns are still moving. The generated patterns are found to move in the direction normal to the symmetry line of electrode shape. In general smaller size pillars are formed when multiple ridges patterned are used as compared to the square block patterns, however, the larger size pillars remained stable for a longer time using square block patterns with negative exposure.

By using patterned mask, smaller size features (with lower characteristic wavelength than the mask patterns) are formed in the combined TC-EHD- as compared to the EHD-induced pattering. Hence, applying TC-EHD is more beneficial than EHD when the replicated features have similar wavelength of the mask. It is anticipated that the results of this study will provide a better understanding of the strengths and limitations present in the TC-EHD compared to the EHD patterning process. This, consequently, enables the formation of high-resolution features which are highly demanded in semi-conductor industries.

DOI: 10.1021/acs.iecr.7b02814
Ind. Eng. Chem. Res. 2017, 56, 10678–10688

AUTHOR INFORMATION

Corresponding Author

*E-mail: sadrzade@ualberta.ca. Tel: +1 780 4928745.

ORCID

Hadi Nazaripoor: 0000-0002-7429-4502

Charles R. Koch: 0000-0002-6094-5933

Notes

The authors declare no competing financial interest.

REFERENCES

(1) Mukherjee, R.; Sharma, A. Instability, self-organization and pattern formation in thin soft films. *Soft Matter* **2015**, *11*, 8717−8740.

(2) Kalpathy, S. K.; Francis, L. F.; Kumar, S. Thin-film models of liquid displacement on chemically patterned surfaces for lithographic printing processes. *J. Colloid Interface Sci.* **2012**, *383*, 155−166.

(3) Wu, N.; Russel, W. B. Micro- and nano-patterns created via electrohydrodynamic instabilities. *Nano Today* **2009**, *4*, 180−192.

(4) Singer, J. P. Thermocapillary approaches to the deliberate patterning of polymers. *J. Polym. Sci., Part B: Polym. Phys.* **2017**, DOI: 10.1002/polb.24298.

(5) Swan, J. W. Stress and other Effects Produced in Resin and in a Viscid Compound of Resin and Oil by Electrification. *Proc. R. Soc. London* **1897**, *62*, 38−46.

(6) Schaffer, E.; Thurn-Albrecht, T.; Russell, T. P.; Steiner, U. Electrically induced structure formation and pattern transfer. *Nature* **2000**, *403*, 874−877.

(7) Lau, C. Y.; Russel, W. B. Fundamental limitations on ordered electrohydrodynamic patterning. *Macromolecules* **2011**, *44*, 7746−7751.

(8) Gambhire, P.; Thaokar, R. Linear Stability Analysis of Electrohydrodynamic Instabilities at Fluid Interfaces in the Small Feature Limit. *Eur. Phys. J. E: Soft Matter Biol. Phys.* **2011**, *34*, 1−12.

(9) Gambhire, P.; Thaokar, R. M. Role of Conductivity in the Electrohydrodynamic Patterning of Air-Liquid Interfaces. *Phys. Rev. E: Stat., Nonlinear, Soft Matter Phys.* **2012**, *86*, 036301.

(10) Yang, Q.; Li, B. Q.; Ding, Y.; Shao, J. Steady State of Electrohydrodynamic Patterning of Micro/Nanostructures on Thin Polymer Films. *Ind. Eng. Chem. Res.* **2014**, *53*, 12720−12728.

(11) Rickard, J. J. S.; Farrer, I.; Oppenheimer, P. G. Tunable nanopatterning of conductive polymers via electrohydrodynamic lithography. *ACS Nano* **2016**, *10*, 3865−3870.

(12) Wang, C.; Shao, J.; Tian, H.; Li, X.; Ding, Y.; Li, B. Q. Step-controllable electric-field-assisted nanoimprint lithography for uneven large-area substrates. *ACS Nano* **2016**, *10*, 4354−4363.

(13) Tian, H.; Shao, J.; Chen, X.; Wang, L.; Ding, Y. A versatile approach to fabricate modulated micro-/nanostructures by electrohydrodynamic structuring on prepatterned polymer. *J. Micromech. Microeng.* **2017**, *27*, 025008.

(14) Tian, H.; Shao, J.; Chen, X.; Jiang, W.; Wang, L.; Ding, Y. Investigation of the role of template features on the electrically induced structure formation (EISF) for a faithful duplication. *Electrophoresis* **2017**, *38*, 1105−1112.

(15) Roberts, S. A.; Kumar, S. AC Electrohydrodynamic Instabilities in Thin Liquid Films. *J. Fluid Mech.* **2009**, *631*, 255−279.

(16) Espin, L.; Corbett, A.; Kumar, S. Electrohydrodynamic instabilities in thin viscoelastic films - AC and DC fields. *J. Non-Newtonian Fluid Mech.* **2013**, *196*, 102−111.

(17) Pease, L. F., III; Russel, W. B. Electrostatically induced submicron patterning of thin perfect and leaky dielectric films: a generalized linear stability analysis. *J. Chem. Phys.* **2003**, *118*, 3790−3803.

(18) Craster, R. V.; Matar, O. K. Electrically induced pattern formation in thin leaky dielectric films. *Phys. Fluids* **2005**, *17*, 1131−1198.

(19) Nazaripoor, H.; Koch, C. R.; Sadrzadeh, M.; Bhattacharjee, S. Electrohydrodynamic patterning of ultra-thin ionic liquid films. *Soft Matter* **2015**, *11*, 2193−2202.

(20) Nazaripoor, H.; Koch, C. R.; Sadrzadeh, M.; Bhattacharjee, S. Compact Micro/Nano Electrohydrodynamic Patterning: Using a Thin Conductive Film and a Patterned Template. *Soft Matter* **2016**, *12*, 1074−1084.

(21) Bandyopadhyay, D.; Sharma, A.; Thiele, U.; Reddy, P. D. S. Electric-Field-Induced Interfacial Instabilities and Morphologies of Thin Viscous and Elastic Bilayers. *Langmuir* **2009**, *25*, 9108−9118.

(22) Gambaryan-Roisman, T. Modulation of Marangoni convection in liquid films. *Adv. Colloid Interface Sci.* **2015**, *222*, 319−331 (Reinhard Miller, Honorary Issue).

(23) Davis, S. H. Thermocapillary instabilities. *Annu. Rev. Fluid Mech.* **1987**, *19*, 403−435.

(24) Oron, A.; Rosenau, P. On a Nonlinear Thermocapillary Effect in Thin Liquid Layers. *J. Fluid Mech.* **1994**, *273*, 361−374.

(25) Oron, A.; Davis, S. H.; Bankoff, S. G. Long-scale evolution of thin liquid films. *Rev. Mod. Phys.* **1997**, *69*, 931−980.

(26) Chou, S. Y.; Zhuang, L. Lithographically induced self-assembly of periodic polymer micropillar arrays. *J. Vac. Sci. Technol., B: Microelectron. Process. Phenom.* **1999**, *17*, 3197−3202.

(27) Schaffer, E.; Harkema, S.; Roerdink, M.; Blossey, R.; Steiner, U. Thermomechanical lithography: pattern replication using a temperature gradient driven instability. *Adv. Mater.* **2003**, *15*, 514−517.

(28) Dietzel, M.; Troian, S. M. Stress and other effects produced in resin and in a viscid compound of resin and oil by electrification. *J. Appl. Phys.* **2010**, *108*, 074308.

(29) McLeod, E.; Liu, Y.; Troian, S. M. Experimental verification of the formation mechanism for pillar arrays in nanofilms subject to large thermal gradients. *Phys. Rev. Lett.* **2011**, *106*, 175501.

(30) Corbett, A.; Kumar, S. Combined thermal and electrohydrodynamic patterning of thin liquid films. *J. Eng. Math.* **2013**, 1−16.

(31) Nazaripoor, H.; Koch, C. R.; Sadrzadeh, M.; Bhattacharjee, S. Thermo-electrohydrodynamic patterning in nanofilms. *Langmuir* **2016**, *32*, 5776−5786.

(32) Pease, L. F.; Russel, W. B. Limitations on Length Scales for Electrostatically Induced Submicrometer Pillars and Holes. *Langmuir* **2004**, *20*, 795−804.

(33) Verma, R.; Sharma, A.; Kargupta, K.; Bhaumik, J. Electric Field Induced Instability and Pattern Formation in Thin Liquid Films. *Langmuir* **2005**, *21*, 3710−3721.

(34) Atta, A.; Crawford, D. G.; Koch, C. R.; Bhattacharjee, S. Influence of Electrostatic and Chemical Heterogeneity on the Electric-Field-Induced Destabilization of Thin Liquid Films. *Langmuir* **2011**, *27*, 12472−12485.

(35) Li, H.; Yu, W.; Zhang, L.; Liu, Z.; Brown, K. E.; Abraham, E.; Cargill, S.; Tonry, C.; Patel, M. K.; Bailey, C.; Desmulliez, M. P. Y. Simulation and modelling of sub-30 nm polymeric channels fabricated by electrostatic induced lithography. *RSC Adv.* **2013**, *3*, 11839−11845.

(36) Yang, Q.; Li, B. Q.; Ding, Y. Dynamic Modelling of Micro/Nano-patterning Transfer by an Electric Field. *RSC Adv.* **2013**, *3*, 24658−24663.

(37) Li, H.; Yu, W.; Wang, Y.; Bu, H.; Liu, Z.; Abraham, E.; Desmulliez, M. P. Y. Simulation of the electrohydrodynamic instability process used in the fabrication of hierarchic and hollow micro/nanostructures. *RSC Adv.* **2014**, *4*, 13774−13781.

(38) Lee, S.; Jung, S. H.; Kang, D. J.; Lee, J. Fabrication of a nanoscale pattern with various functional materials using electrohydrodynamic lithography and functionalization. *RSC Adv.* **2016**, *6*, 5944−5948.

(39) Li, W.; Carvalho, M. S.; Kumar, S. Liquid-film coating on topographically patterned rotating cylinders. *Phys. Rev. Fluids* **2017**, *2*, 024001.

(40) Wu, N.; Pease, L.; Russel, W. Toward Large-Scale Alignment of Electrohydrodynamic Patterning of Thin Polymer Films. *Adv. Funct. Mater.* **2006**, *16*, 1992−1999.

(41) Tian, H.; Shao, J.; Ding, Y.; Li, X.; Liu, H. Numerical Characterization of Electrohydrodynamic Micro- or Nanopatterning Processes Based on a Phase-Field Formulation of Liquid Dielectrophoresis. *Langmuir* **2013**, *29*, 4703−4714.

DOI: 10.1021/acs.iecr.7b02814
Ind. Eng. Chem. Res. 2017, 56, 10678−10688

(42) Tian, H.; Wang, C.; Shao, J.; Ding, Y.; Li, X. Electrohydrodynamic Pressure Enhanced by Free Space Charge for Electrically Induced Structure Formation with High Aspect Ratio. *Langmuir* **2014**, *30*, 12654−12663.
(43) Israelachvili, J. N. *Intermolecular and Surface Forces*; Academic Press: Burlington, MA, 2011.
(44) Dietzel, M.; Troian, S. M. Formation of Nanopillar Arrays in Ultrathin Viscous Films: The Critical Role of Thermocapillary Stresses. *Phys. Rev. Lett.* **2009**, *103*, 074501.
(45) Nazaripoor, H.; Koch, C. R.; Bhattacharjee, S. Electrical perturbations of ultrathin bilayers: role of ionic conductive layer. *Langmuir* **2014**, *30*, 14734−14744.
(46) Lin, Z.; Kerle, T.; Russell, T. P.; Schäffer, E.; Steiner, U. Structure formation at the interface of liquid/liquid bilayer in electric field. *Macromolecules* **2002**, *35*, 3971−3976.
(47) Brenan, K. E.; Petzold, L. R. The numerical solution of higher index differential/algebraic equations by implicit methods. *SIAM J. Numer. Anal.* **1989**, *26* (4), 976−996.
(48) Wu, N.; Russel, W. B. Electrohydrodynamic instability of dielectric bilayers: kinetics and thermodynamics. *Ind. Eng. Chem. Res.* **2006**, *45*, 5455−5465.

DOI: 10.1021/acs.iecr.7b02814
Ind. Eng. Chem. Res. 2017, 56, 10678−10688